Title

Label-free assessment of carotid artery biochemical composition using fiber-based fluorescence lifetime imaging

Journal

Biomedical Optics Express, 9(9)

ISSN

2156-7085

Authors

Alfonso-Garcia, Alba
Haudenschild, Anne K
Marcu, Laura

Publication Date

2018-09-01

DOI

10.1364/boe.9.004064

Peer reviewed

Research Article | Vol. 9, No. 9 | 1 Sep 2018 | BIOMEDICAL OPTICS EXPRESS 4064
Biomedical Optics EXPRESS

Label-free assessment of carotid artery biochemical composition using fiber-based fluorescence lifetime imaging

ALBA ALFONSO-GARCIA,[1,2] ANNE K. HAUDENSCHILD,[1,2] AND LAURA MARCU[1,*]

[1]*Department of Biomedical Engineering, University of California, Davis, 451 E. Health Sciences Dr., Davis, CA 95616, USA*
[2]*Authors contributed equally to this work*
[*]*lmarcu@ucdavis.edu*

Abstract: Novel diagnostic tools with the ability to monitor variations in biochemical composition and provide benchmark indicators of vascular tissue maturation are needed to create functional tissue replacements. We investigated the ability of fiber-based, label-free multispectral fluorescent lifetime imaging (FLIm) to quantify the anatomical variations in biochemical composition of native carotid arteries and validated these results against biochemical assays. FLIm-derived parameters in spectral band 415–455 nm correlated with tissue collagen content ($R^2 = 0.64$) and cell number ($R^2 = 0.61$) and in spectral band 465–553 nm strongly correlated with elastin content ($R^2 = 0.89$). These results suggest that FLIm holds great potential for assessing vascular tissue maturation and functional properties based on tissue autofluorescence.

OCIS codes: (060.2350) Fiber optics imaging; (170.3880) Medical and biological imaging; (170.6920) Time-resolved imaging.

References and links

1. S. L. Dahl, C. Rhim, Y. C. Song, and L. E. Niklason, "Mechanical Properties and Compositions of Tissue Engineered and Native Arteries," Annals Biomed. Eng. **35**, 348–355 (2007).
2. T. C. Rothuizen, F. F. R. Damanik, T. Lavrijsen, M. J. T. Visser, J. F. Hamming, R. A. Lalai, J. M. G. J. Duijs, A. J. van Zonneveld, I. E. Hoefer, C. A. van Blitterswijk, T. J. Rabelink, L. Moroni, and J. I. Rotmans, "Development and evaluation of in vivo tissue engineered blood vessels in a porcine model," Biomaterials. **75**, 82–90 (2016).
3. Y. Sun, Y. Sun, D. Stephens, H. Xie, J. Phipps, R. Saroufeem, J. Southard, D. S. Elson, and L. Marcu, "Dynamic tissue analysis using time- and wavelength-resolved fluorescence spectroscopy for atherosclerosis diagnosis,," Opt. Express **19**, 3890–3901 (2011).
4. K. P. Quinn, E. Bellas, N. Fourligas, K. Lee, D. L. Kaplan, and I. Georgakoudi, "Characterization of metabolic changes associated with the functional development of 3D engineered tissues by non-invasive, dynamic measurement of individual cell redox ratios," Biomaterials **33**, 5341–5348 (2012).
5. D. Gorpas, H. Fatakdawala, J. Bec, D. Ma, D. R. Yankelevich, J. Qi, and L. Marcu, "Fluorescence lifetime imaging and intravascular ultrasound: co-registration study using ex vivo human coronaries," IEEE Trans Med Imaging **34**, 156–166 (2015).
6. D. Gorpas, D. Ma, J. Bec, D. R. Yankelevich, and L. Marcu, "Real-time visualization of tissue surface biochemical features derived from fluorescence lifetime measurements," IEEE Trans. Med. Imaging **35**, 1802–1811 (2016).
7. S. Shrestha, M. J. Serafino, J. Rico-Jimenez, J. Park, X. Chen, S. Zhaorigetu, B. L. Walton, J. A. Jo, and B. E. Applegate, "Multimodal optical coherence tomography and fluorescence lifetime imaging with interleaved excitation sources for simultaneous endogenous and exogenous fluorescence," Biomed. Opt. Express **7**, 3184 (2016).
8. I. Georgakoudi, B. C. Jacobson, M. G. Mu, E. E. Sheets, K. Badizadegan, D. L. Carr-locke, C. P. Crum, C. W. Boone, R. R. Dasari, J. V. Dam, and M. S. Feld, "NAD(P)H and Collagen as in Vivo Quantitative Fluorescent Biomarkers of Epithelial Precancerous Changes," Cancer Res. **62**, 682–687 (2002).
9. G. a. Wagnieres, W. M. Star, and B. C. Wilson, "In Vivo Fluorescence Spectroscopy and Imaging for Oncological Applications," Photochem. Photobiol. **68**, 603–632 (1998).
10. B. E. Sherlock, J. N. Harvestine, D. Mitra, A. Haudenschild, J. Hu, K. A. Athanasiou, J. K. Leach, and L. Marcu, "Nondestructive assessment of collagen hydrogel cross-linking using time-resolved autofluorescence imaging," J. Biomed. Opt. **23**, 1–9 (2018).
11. L. Marcu, P. M. French, and D. S. Elson, *Fluorescence Lifetime Spectroscopy and Imaging: Principles and Applications in Biomedical Diagnostics* (CRC Press, 2014).

#335443 https://doi.org/10.1364/BOE.9.004064
Journal © 2018 Received 18 Jun 2018; revised 11 Jul 2018; accepted 12 Jul 2018; published 6 Aug 2018

Biomedical Optics EXPRESS

12. W. Becker, "Fluorescence lifetime imaging - techniques and applications," J. Microsc. **247**, 119–136 (2012).
13. J. Phipps, Y. Sun, R. Saroufeem, N. Hatami, M. C. Fishbein, and L. Marcu, "Fluorescence lifetime imaging for the characterization of the biochemical composition of atherosclerotic plaques," J. Biomed. Opt. **16**, 096018 (2011).
14. J. Bec, H. Xie, D. R. Yankelevich, F. Zhou, Y. Sun, N. Ghata, R. Aldredge, and L. Marcu, "Design, construction, and validation of a rotary multifunctional intravascular diagnostic catheter combining multispectral fluorescence lifetime imaging and intravascular ultrasound," J. Biomed. Opt. **17**, 106012 (2012).
15. J. Bec, J. E. Phipps, D. Gorpas, D. Ma, H. Fatakdawala, K. B. Margulies, J. A. Southard, and L. Marcu, "In vivo label-free structural and biochemical imaging of coronary arteries using an integrated ultrasound and multispectral fluorescence lifetime catheter system," Sci. Reports **7**, 8690 (2017).
16. S. Liang, A. Saidi, J. Jing, G. Liu, J. Li, J. Zhang, C. Sun, J. Narula, and Z. Chen, "Intravascular atherosclerotic imaging with combined fluorescence and optical coherence tomography probe based on a double-clad fiber combiner," J. Biomed. Opt. **17**, 0705011 (2012).
17. G. S. Mintz, "Intravascular imaging of coronary calcification and its clinical implications," JACC: Cardiovasc. Imaging **8**, 461–471 (2015).
18. T. Ma, M. Yu, Z. Chen, C. Fei, K. K. Shung, and Q. Zhou, "Multi-Frequency Intravascular Ultrasound," IEEE Transactions on Ultrason. Ferroelectr. Freq. Control. **62**, 97–107 (2015).
19. D. Ma, J. Bec, D. R. Yankelevich, D. Gorpas, H. Fatakdawala, and L. Marcu, "Rotational multispectral fluorescence lifetime imaging and intravascular ultrasound: bimodal system for intravascular applications," J. Biomed. Opt. **19**, 066004 (2014).
20. Y. Cao, J. Hui, A. Kole, P. Wang, Q. Yu, W. Chen, M. Sturek, and J. X. Cheng, "High-sensitivity intravascular photoacoustic imaging of lipid-laden plaque with a collinear catheter design," Sci. Rep. **6**, 1–8 (2016).
21. W. R. Milnor, *Hemodynamics* (Williams and Wilkins, 1982).
22. A. García, E. Peña, A. Laborda, F. Lostalé, M. A. De Gregorio, M. Doblaré, and M. A. Martínez, "Experimental study and constitutive modelling of the passive mechanical properties of the porcine carotid artery and its relation to histological analysis: Implications in animal cardiovascular device trials," Med. Eng. Phys. **33**, 665–676 (2011).
23. H. L. Wyatt, R. Richards, R. Pullin, T. J. Yang, E. J. Blain, and S. L. Evans, "Variation in electrosurgical vessel seal quality along the length of a porcine carotid artery," J. Eng. Medicine **230**, 169–174 (2016).
24. H. E. Evans and A. De Lahunta, *Miller's Anatomy of the Dog-E-Book* (Elsevier Health Sciences, 2013).
25. F. R. Nowrozani and B. Zareiyan, "A microscopic study of the external carotid artery transitional zone of the adult male dog," J. Appl. Animal Res. **39**, 406–411 (2011).
26. P. Kochová, J. Kuncová, J. Švíglerová, R. Cimrman, M. Miklíková, V. Liška, and Z. Tonar, "The contribution of vascular smooth muscle, elastin and collagen on the passive mechanics of porcine carotid arteries," Physiol. Meas. **33**, 1335–1351 (2012).
27. J. E. Wagenseil and R. P. Mecham, "Vascular Extracellular Matrix and Arterial Mechanics," Physiol. Rev. **89**, 957–989 (2009).
28. D. Sindram, K. Martin, J. P. Meadows, A. S. Prabhu, J. J. Heath, I. H. McKillop, and D. A. Iannitti, "Collagen–elastin ratio predicts burst pressure of arterial seals created using a bipolar vessel sealing device in a porcine model," Surg. Endosc. **25**, 2604–2612 (2011).
29. M. Dettin, A. Zamuner, F. Naso, A. Monteleone, M. Spina, and G. Gerosa, "Natural scaffolds for regenerative medicine: Direct determination of detergents entrapped in decellularized heart valves," Biomed. Res. Int. **2017**, 9274135 (2017).
30. D. D. Cissell, J. C. Hu, L. G. Griffiths, and K. A. Athanasiou, "Antigen removal for the production of biomechanically functional, xenogeneic tissue grafts," J. Biomech. **47**, 1987–1996 (2014).
31. H. Y. Tuan-Mu, C. H. Yu, and J. J. Hu, "On the decellularization of fresh or frozen human umbilical arteries: implications for small-diameter tissue engineered vascular grafts," Ann. Biomed. Eng. **42**, 1305–1318 (2014).
32. K. Dowling, M. J. Dayel, S. C. W. Hyde, P. M. W. French, M. J. Lever, J. D. Hares, and A. K. L. Dymoke-bradshaw, "High resolution time-domain fluorescence lifetime imaging for biomedical applications," J. Mod. Opt. **46**, 199–209 (1999).
33. L. Marcu, "Characterization of type I, II, III, IV, and V collagens by time-resolved laser-induced fluorescence spectroscopy," Proc. SPIE **3917**, 93–101 (2000).
34. S. Ranjit, A. Dvornikov, M. Stakic, S.-H. Hong, M. Levi, R. M. Evans, and E. Gratton, "Imaging Fibrosis and Separating Collagens using Second Harmonic Generation and Phasor Approach to Fluorescence Lifetime Imaging," Sci. Reports **5**, 13378 (2015).
35. R. T. Venkatasubramanian, W. F. Wolkers, M. M. Shenoi, V. H. Barocas, D. Lafontaine, C. L. Soule, P. A. Iaizzo, and J. C. Bischof, "Freeze-thaw induced biomechanical changes in arteries: Role of collagen matrix and smooth muscle cells," Annals Biomed. Eng. **38**, 694–706 (2010).
36. A. Ozcelikkale and B. Han, "Thermal destabilization of collagen matrix hierarchical structure by freeze/thaw," PLoS ONE **11** (2016).
37. M. M. Swindle and A. C. Smith, *Swine in the laboratory* (CRC Press, Boca Raton, 2016), 3rd ed.
38. A. Alfonso-Garcia, J. Shklover, B. E. Sherlock, A. Panitch, L. G. Griffiths, and L. Marcu, "Fiber-based fluorescence lifetime imaging of recellularization processes on vascular tissue constructs," J Biophotonics p. e201700391 (2018).
39. J. Kim, M. Lee, J. H. Yang, and J. H. Choy, "Photophysical Properties of Hemicyanine Dyes Intercalated in Na - Fluorine Mica," J. Phys. Chem. A **104**, 1388–1392 (2000).

Biomedical Optics EXPRESS

40. P. Pande and J. A. Jo, "Automated analysis of fluorescence lifetime imaging microscopy (FLIM) data based on the laguerre deconvolution method," IEEE Transactions on Biomed. Eng. **58**, 172–181 (2011).
41. D. R. Yankelevich, D. Ma, J. Liu, Y. Sun, Y. Sun, J. Bec, D. S. Elson, and L. Marcu, "Design and evaluation of a device for fast multispectral time-resolved fluorescence spectroscopy and imaging," Rev. Sci. Instruments **85**, 034303 (2014).
42. A. Sillen and Y. Engelborghs, "The Correct Use of "Average" Fluorescence Parameters," Photochem. Photobiol. **67**, 475–486 (1998).
43. J. R. Lakowicz, *Principles of Fluorescence Spectroscopy, 3rd Edition* (Springer, 2006).
44. G. E. Kochiadakis, S. I. Chrysostomakis, M. D. Kalebubas, G. M. Filippidis, I. G. Zacharakis, T. G. Papazoglou, and P. E. Vardas, "The role of laser-induced fluorescence in myocardial tissue characterization: an experimental in vitro study," Chest. **120**, 233–239 (2001).
45. M. L. Wong, J. L. Wong, K. A. Athanasiou, and L. G. Griffiths, "Stepwise solubilization-based antigen removal for xenogeneic scaffold generation in tissue engineering," Acta Biomater. **9**, 6492–6501 (2013).
46. J. F. Gillooly, A. Hein, and R. Damiani, "Nuclear DNA Content Varies with Cell Size across Human Cell Types," Cold Spring Harb. Perspect. Biol. **7**, 1–28 (2015).
47. S. Roy, P. Silacci, and N. Stergiopulos, "Biomechanical proprieties of decellularized porcine common carotid arteries Sylvain," Am. J. Physiol. Hear. Circ. Physiol. **289**, H1567–H1576 (2005).
48. J. M. Maarek, L. Marcu, W. J. Snyder, and W. S. Grundfest, "Time-resolved fluorescence spectra of arterial fluorescent compounds: reconstruction with the Laguerre expansion technique," Photochem. Photobiol. **71**, 178–187 (2000).
49. S. Andersson-Engels, J. Johansson, K. Svanberg, and S. Svanberg, "Fluorescence imaging and point measurements of tissue: applications to the demarcation of malignant tumors and atherosclerotic lesions from normal tissue," Photochem. Photobiol. **53**, 807–814 (1991).
50. D. Sindram, K. Martin, J. P. Meadows, A. S. Prabhu, J. J. Heath, I. H. McKillop, and D. A. Iannitti, "Collagen-elastin ratio predicts burst pressure of arterial seals created using a bipolar vessel sealing device in a porcine model," Surg. Endosc. Other Interv. Tech. **25**, 2604–2612 (2011).
51. S. A. O'Leary, B. J. Doyle, and T. M. McGloughlin, "The impact of long term freezing on the mechanical properties of porcine aortic tissue," J. Mech. Behav. Biomed. Mater. **37**, 165–173 (2014).

1. Introduction

New diagnostic tools for the quantitative analysis of biological variation within native and tissue-engineered vascular tissues are needed to create functional tissue replacements. Currently, tissue engineers rely predominantly on destructive and time-consuming techniques that require complete or partial sample loss to determine tissue quality [1, 2]. An imaging system capable of evaluating the spatial and temporal changes in biochemical content in a number of research environments would greatly advance the development of vascular tissue-engineered constructs that mimic native tissue.

In an effort to address this need, quantitative optical techniques based on endogenous tissue autofluorescence have been developed to image and nondestructively characterize tissue properties [3–7]. A number of endogenous biomolecules, including proteins of the extracellular matrix (ECM) like collagen [8], collagen crosslinks [9, 10] and elastin [11], give rise to tissue autofluorescence. Fluorescence Lifetime Imaging (FLIm) is an imaging technique that uses differences in the exponential decay rate of tissue autofluorescence to generate images of tissue biochemical content [11, 12] that can be associated with tissue functional properties. Unlike fluorescence lifetime imaging microscopy (FLIM) that utilizes microscope objectives, FLIm utilizes a single, narrow and flexible fiber-optic interface between the imaging system and the sample and has been shown individually to detect biochemical changes in various biological tissues, both *in vitro* and *in vivo* [13–15]. In addition, FLIm is compatible with other imaging techniques that complement the biochemical information with a structural description of the sample, such as optical coherence tomography [7, 10, 16, 17], intravascular ultrasound [15, 17–19], and intravascular photoacoustics [20].

In this study, we utilize the naturally occurring anatomical differences in ECM composition of healthy carotid arteries [21–23] as an experimental model for developing novel diagnostic techniques. The two external carotid arteries are the principal arteries supplying the head and neck [24]. Moving along the length of each artery from the heart (caudal region) toward the head (cranial region) there is an arterial narrowing and a distinct transitional zone in which the elastic

Biomedical Optics EXPRESS

wall is replaced by a muscular type [25], resulting in the caudal region of the artery having a larger elastin content and the cranial region a more collagenous structure. Collagen and elastin are the main components responsible for the mechanical behavior of the arterial wall [26, 27] and alterations in the collagen to elastin ratio help maintain blood pressure and regulate blood flow across changes in artery diameter [25, 28]. An imaging technique that quantitatively assess the anatomical differences in the collagen and elastin content of native artery would provide direct biochemical information and also infer differences in the functional properties of the tissue. To minimize the disruption of vascular tissue during evaluation, fiber-based instruments are ultimately required for examining native vessels in their local environment (*in vivo*) and engineered vascular tissue grown in bioreactors (*in vitro*).

Cryopreservation and chemical processing of tissue engineered vascular grafts derived from both human and animal tissues are currently used in clinical applications of vascular repair [29–31]. The absolute fluorescence lifetime values of elastin and collagen vary significantly depending on sample preparation, storage, and environment, and the fluorescence lifetime values of elastin and collagen solutions differ from those in native tissue [32–34]. In addition, tissue freezing results in altered collagen structure due to the expansion of intra-fibrillar fluid during ice formation [35, 36] and cell death. Characterizing the subsequent changes in optical properties that occur with freezing is important for accurate interpretation of experimental results and comparison to data published in the literature.

The overall objective of this work is to study whether fiber-based FLIm has the potential to assess spatial changes in biochemical composition in healthy carotid arteries. In this study, we utilized the naturally occurring anatomical differences in collagen and elastin content of carotid arteries [21] as an experimental model to form specific, quantitative relationships between FLIm-derived parameters and tissue biochemical properties. In addition, we studied the effect of tissue freezing on fluorescent parameters. By examining a range of biochemical properties, we determined which optical parameters are best suited for collagen and elastin quantification and whether the strength of these correlations are sufficient to characterize artery biochemical composition. We showed that label-free FLIm can be used to determine the spatial changes in biochemical composition of carotid arteries over a range of matrix compositions and that these relationships are significantly altered with tissue processing.

2. Materials and methods

2.1. Carotid artery processing

Porcine carotid arteries (PCA) (4 - 10 cm in length, 3 - 5 mm in diameter, 600 - 800 μm thick) were harvested from the external carotid artery cranial to the point of bifurcation in domestic pigs (ranging from 39 - 128 kg in weight, ~ 3 - 8 months in age [37]) immediately following sacrifice (UC Davis Meat Lab, Davis, CA), trimmed of surrounding tissue, and incised longitudinally to expose the luminal side (n = 11). Samples were stored in phosphate buffered saline (PBS) (Sigma-Aldrich, St. Louis, MO) prior to optical evaluation. A subset of matched samples (n = 4 animals labeled P1 - P4; 2 anatomical locations) were further processed for biochemical and histological analysis (Fig. 1(a); Overview). All samples were imaged within one hour of sacrifice. For comparison of viable and frozen tissue optical properties, a subset of freshly harvested samples (n = 3) were imaged immediately (viable) and after three freeze-thaw cycles at -20 °C (frozen).

2.2. Fluorescence lifetime imaging

Label-free FLIm was performed with a fiber-based multispectral instrument previously described [38]. Briefly, pulse sampling in the time domain was used to retrieve fluorescence spectral and lifetime (LT) properties from the exposed lumen of the carotid arteries, positioned 0.5 - 1.0 mm

Biomedical Optics EXPRESS

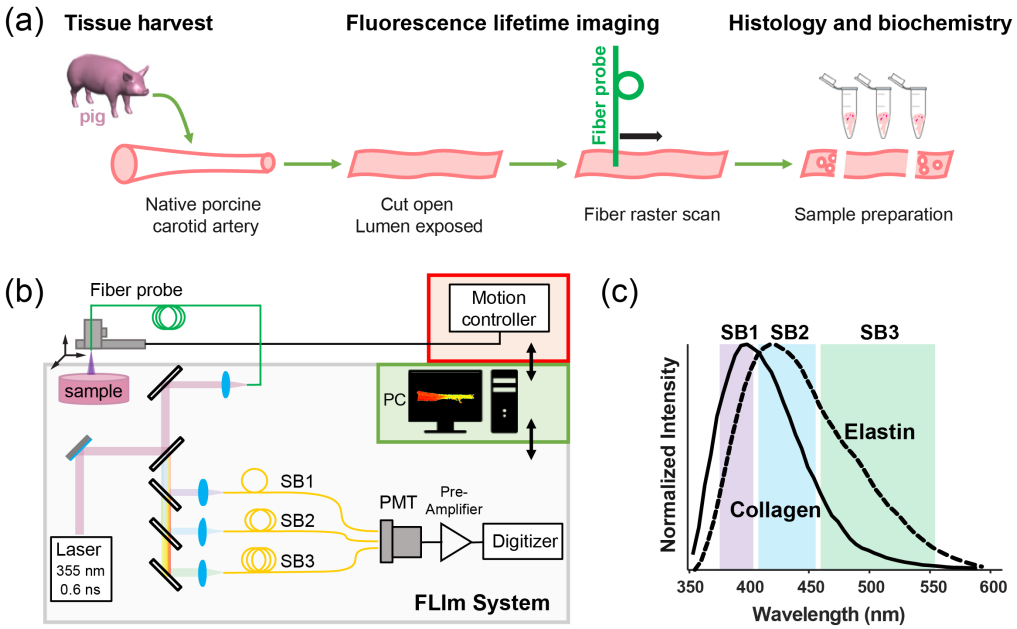

Fig. 1. (a) Schematic of sample preparation, imaging and biochemical evaluation. (b) Schematic of the FLIm system. (c) Spectral signatures of collagen and elastin, and identification of the used spectral bands, SB1: 380 - 400 nm, SB2: 415 - 455 nm, SB3: 465 - 553 nm.

away from the fiber tip. The instrument consisted of a 355 nm Q-switched microchip pulsed laser (pulse duration < 0.6 ns, pulse energy > 2 μJ, repetition rate 4kHz; TEEM photonics STV-02E, Meylan, France) coupled to a 400 μm core multimode fiber that was raster scanned across the surface of the sample with a 3-axis translation stage (PROmech LP28, Parker, Charlotte, NC). Tissue autofluorescence was collected back through the same multimode fiber and delivered to a set of dichroic mirrors and filters that spectrally separated the collected light into three different spectral bands (SB) (Table 1). Each SB was coupled to a fiber optic delay line of progressively increasing length to temporally multiplex the signal in a single microchannel plate photomultiplier tube (MCP-PMT; R3809U-50, Hamamatsu, Japan), connected to a high speed digitizer (12.5 GS/s, 3 GHz bandwidth; NI PXIe-5185, National Instruments, Austin, TX) (Fig. 1(b)).

The spectral bands defined in Table 1 cover the emission spectra of the main structural proteins in carotid arteries, i.e. collagen and elastin, as depicted in Fig. 1(c).

Table 1. **Assignation of spectral bands in the multispectral FLIm instrument.**

Spectral band label	Spectral range
SB1	380 - 400 nm
SB2	415 - 455 nm
SB3	465 - 553 nm

Images sized ~ 80 mm x 25 mm were acquired with square pixels of 200 μm x 200 μm, in about 5 minutes. The penetration depth of this setup is estimated to be < 300 μm. The instrument response function was measured after each imaging session using the decay of 2-DASPI (2-[4-(dimethylamino)styryl]-1-methylpyridinium iodide (Sigma-Aldrich) that has an

Biomedical Optics EXPRESS

average fluorescence lifetime of 30 ps when dissolved in ethanol [19, 39].

The data processing pipeline was based on a constrained least square deconvolution with expansion into the Laguerre basis functions, as previously detailed [40,41]. The retrieved metrics of interest for each spectral bands are the intensity ratio (IR), computed as the area under the waveform for each band divided by the contribution from all spectral bands (Eq. 1), and the average fluorescence lifetime (τ_{avg}), interpreted as the expectation value of the probability density function of the fluorescence decay (Eq. 2) [42,43].

$$IR_i = \frac{I_i}{\sum_{j=1}^{3} I_j}, \quad i = 1, 2, 3 \tag{1}$$

$$\tau_{avg} = \frac{\int_0^\infty t \cdot I(t)dt}{\int_0^\infty I(t)dt} \tag{2}$$

2.3. Biochemical analysis and histology

After fluorescence lifetime imaging, full-thickness tissue was collected from the cranial and caudal regions of the carotid artery (n = 4 animals) using a 6 mm diameter dermal biopsy punch. Arteries were photographed after sample harvest to define FLIm data regions of interest and lyophilized for 4 days to create matched samples for biochemical analysis. Minced lyophilized samples were weighed to determine dry weight (DW) and 20 mg of each sample was used for elastin quantification using a quantitative dye-binding Fastin Elastin Assay (Biocolor, Carrickfergus, UK). Briefly, native, hydrophobic elastin was converted to soluble α-elastin by hot acid extraction, precipitated and treated with the dye 5,10,15,20-tetraphenyl-21H,23H-porphine tetra-sulfonate (TPPS) that binds to elastin, and measured at 510 nm. The amount of α-elastin (μg) in each sample was calculated from the linear fit of standard curve of elastin, normalized to dry weight, and expressed as elastin content.

For collagen and DNA analysis, lyophilized samples were digested in papain for 18 h at 60 °C, as previously described [44]. Total collagen content was quantified using a chloramine-T hydroxyproline assay (Biocolor), as previously described [45]. The collagen content of each sample was normalized to dry weight and expressed as collagen content. Total DNA was quantified using a fluorescent PicoGreen dsDNA assay (Molecular Probes, Eugene, OR). Cell number was calculated from DNA results using 7.9 pg DNA / cell [46]. The calculated cell number of each sample was normalized to dry weight and expressed as cell content.

For histological evaluation, full-width, cross-sectional cuts from the cranial and caudal regions of each artery were fixed in 10 % neutral buffered formalin, paraffin embedded, sectioned at 10 μm, and stained with Verhoeff –Van Gieson stain (VVG) for elastin, or picrosirius red and nuclear fast green for total collagen following routine procedures.

2.4. Statistical analysis and modeling

All FLIm evaluations in this study were performed using n = 11 animals. Data are presented as mean ± standard deviation computed from regions of interest defined in either region of the arteries (cranial and caudal). For comparison between anatomical locations, a pooled t-test was used and significant differences ($p < 0.05$) are indicated by an asterisk. To determine correlations between optical parameters and biochemical components, simple linear least squares regression analysis was performed on a subset of matched samples (n = 4 animals; 2 anatomical locations). Bivariate linear regression model data are presented with the R^2, root mean square error (RMSE), and the *p-value* for significant differences ($p < 0.05$) (Fig. 4(a)-(c)). To determine which biochemical components have significant effects on imaging properties, multivariable linear regression modeling was performed using multiple independent variables (normalized collagen, elastin, cell number, animal, anatomical location) against each single dependent outcome

Biomedical Optics EXPRESS

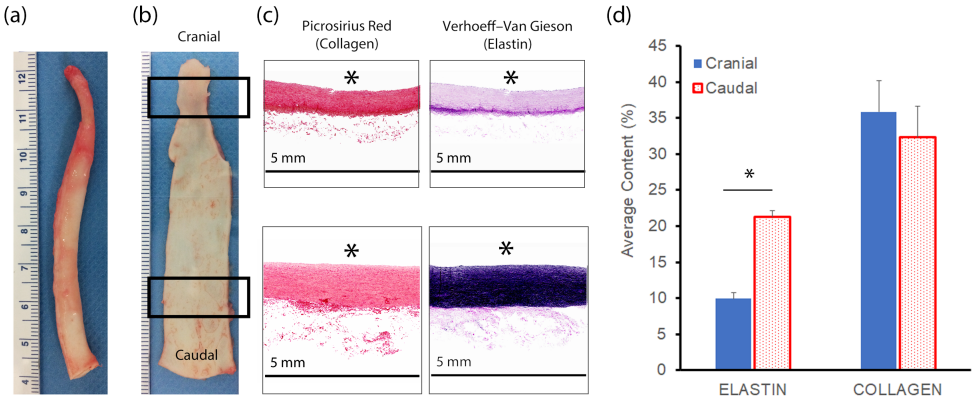

Fig. 2. Anatomical variations in porcine carotid artery biochemical composition. (a) Representative native porcine carotid artery shows narrowing from caudal (bottom) to cranial (top) regions. (b) Longitudinal incision to expose the lumen for imaging. (c) Representative picrosirius red staining (left) and Verhoeff-Van Gieson staining (right) staining of two different anatomical regions within the artery (caudal - bottom and cranial - top) as indicated corresponding to black squared regions (* denotes luminal side). (d) Quantification of collagen and elastin composition confirms significant anatomical variations in extracellular matrix biochemical composition.

measurement (SB1 LT, SB2 LT, SB3 LT, IR1, IR2, IR3) (Fig. 4(d)). Multivariable regression model data are presented with the predicted response as a solid black line, the 95 % confidence interval as blue curves, and the *p-value* for significant differences ($p < 0.05$) (Fig. 4(d)). For comparison between viable and frozen arteries (n=3), a matched t-test was used and significant differences ($p < 0.05$) are indicated by an asterisk. All statistical analyses were performed on JMP Pro v14 (SAS Institute, Cary, NC).

3. Results

3.1. Biochemical composition of carotid artery varies across anatomical locations

Excised porcine carotid arteries showed a sharp reduction in diameter in the cranial region as compared to the caudal region of the artery (Fig. 2(a)–(b)). Histological evaluation showed the caudal region of the artery had qualitatively low picrosirius red staining for collagen and very strong Verhoeff–Van Gieson staining for elastin. In contrast, the cranial region had qualitatively higher picrosirius red staining and very low Verhoeff–Van Gieson staining. Quantification of elastin showed over a 2-fold significant increase in elastin content in the caudal region as compared to the cranial region ($p < 0.001$). Quantification of collagen showed a non–significant decrease in collagen content in the caudal region as compared to the cranial region ($p = 0.19$) (Fig. 2(d)). Normalized cell content significantly decreased in the caudal region as compared to the cranial region ($p = 0.02$; Δ = 2,580 ± 700 cells / DW).

3.2. FLIm-derived parameters detect biochemical changes associated with anatomical locations

Anatomical changes along the length of porcine carotid arteries give rise to distinct fluorescence properties that are captured by FLIm. The two anatomical regions of the arteries are clearly differentiated by a sharp transition where the arterial diameter narrows. Statistical modeling

Biomedical Optics EXPRESS

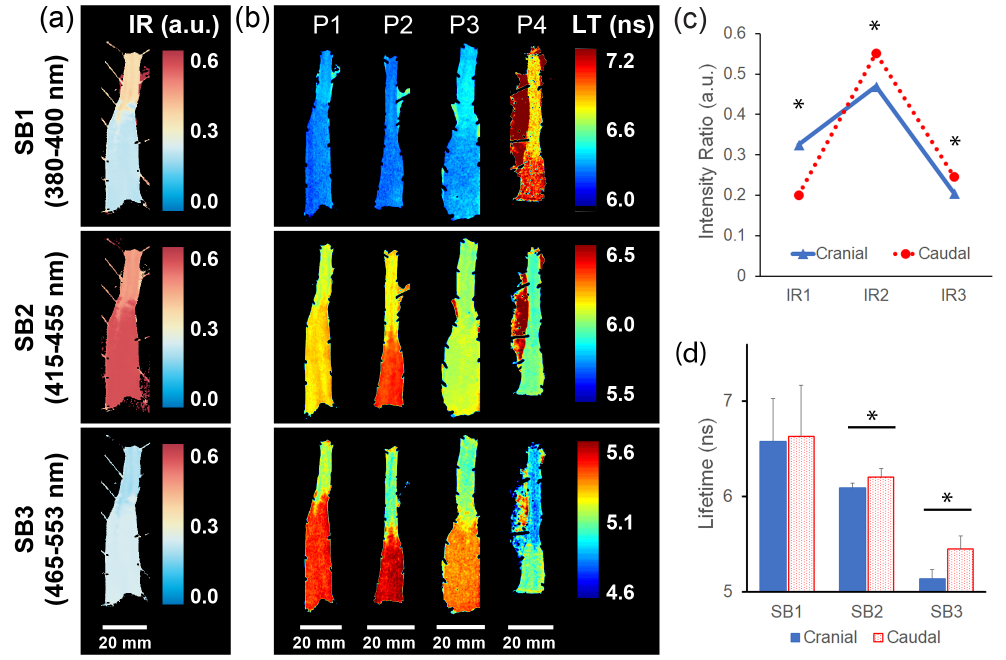

Fig. 3. FLIm analysis detects anatomical variations in porcine carotid artery. (a) Fluorescence intensity ratio (IR) images of a representative carotid artery in the three spectral bands (SB). (b) Fluorescence lifetime (LT) images of four representative carotid arteries in the three SB from three large pigs (P1-P3) and one smaller pig (P4). Average intensity ratios (c), and fluorescence lifetime (d) quantification for each spectral band in the cranial and the caudal regions of the arteries (n = 11).

determined that both animal and anatomical location had significant effects on all FLIm-derived parameters ($p < 0.001$ for all). Fluorescence intensity variations in each spectral band is shown in the IR maps (Fig. 3(a); representative artery). The strongest intensity was always detected in the spectral range 415-455 nm (IR2). IR1 in the cranial region was stronger than for the caudal region (Fig. 3(c)). The differences in intensity ratio between the two regions of the artery were significant for all the spectral bands utilized in this study ($p < 0.0001$), and where found to be binary rather than gradual in the transition zone.

The fluorescence lifetime maps of four representative carotid arteries (P1-P4) are shown in Fig. 3(b) and summarized in Table 2. Animals for samples P1 through P3 were similar in weight (~ 128 kg), while P4 was from a much smaller pig (~ 39 kg). The highest lifetime values were obtained in SB1, with no significant differences between the cranial and the caudal regions. The fluorescence lifetime measured in SB2 were slightly shorter but significantly varied between anatomical locations. On average, there was a difference of 100 ps between the two anatomical regions. Differences were highly animal dependent, as illustrated in Fig. 3(b); some carotid arteries exhibited negligible differences from end to end (e.g. P3 and P4), while others differed up to 200 ps (e.g. P1 and P2). The changes were most remarkable at longer wavelengths (SB3). For this spectral band, the difference in fluorescence LT between the cranial and the caudal region of the artery could be as small as 90 ps or as large as 500 ps. The longest fluorescent LT values were always found on the caudal region. According to LT values, the transition zone between the cranial and the caudal zone was either negligible (e.g. P2 SB1) or abrupt (e.g. P1 SB3). Sample P4 shows an area with even higher fluorescence lifetime values in SB1 and SB2 on the

Biomedical Optics EXPRESS

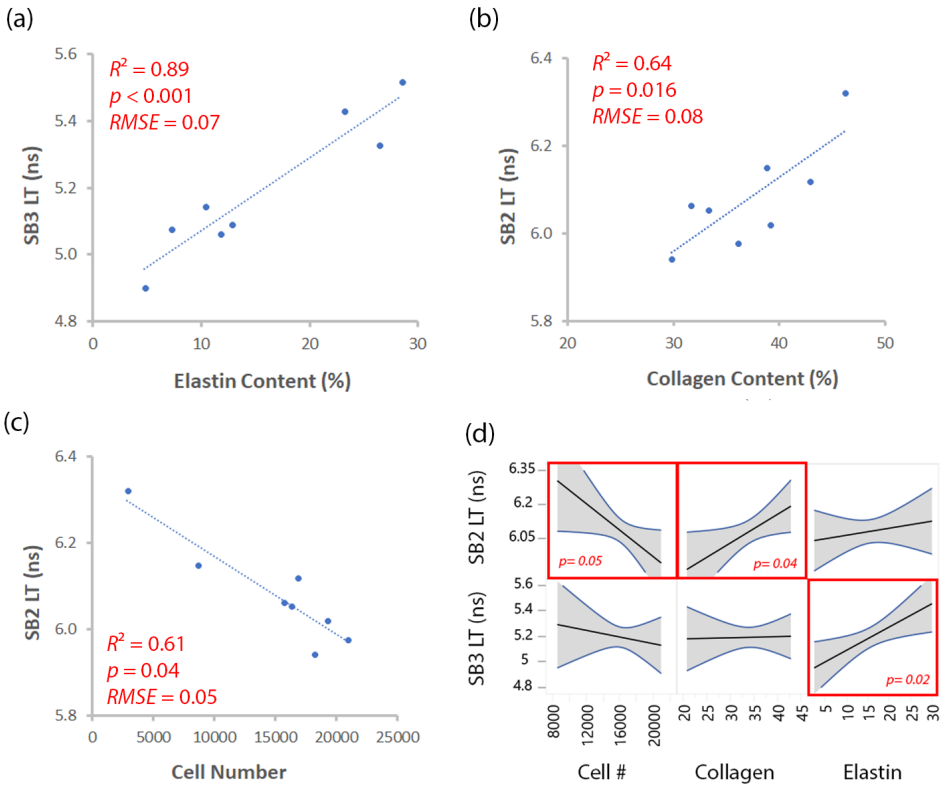

Fig. 4. FLIm-derived parameters are sensitive to tissue composition. Linear correlations between (a) SB3 LT and elastin content, (b) SB2 LT and collagen content, and (c) SB2 LT and cell number. (d) Multivariable linear regression model of all biochemical components against FLIm LT data.

left hand-side of the vessel corresponding to fatty tissue that was attached to the adventitial side of the artery.

Table 2. **Anatomical variation in fluorescence lifetime values of pig carotid arteries (mean ± std; matched t-test *p*-values; n = 11).**

Spectral band	Cranial LT (ns)	Caudal LT (ns)	*p*-value
SB1	6.6 ± 0.5	6.6 ± 0.5	0.79
SB2	6.09 ± 0.05	6.2 ± 0.1	**0.0007**
SB3	5.14 ± 0.09	5.5 ± 0.1	**< 0.0001**

3.3. *FLIm-derived parameters are sensitive to changes in carotid artery extracellular matrix and correlate with biochemical assays*

Bivariate analysis of PCA samples revealed significant, linear correlations between SB3 LT and elastin content (Fig. 4(a), $R^2 = 0.89$, $p < 0.001$), SB2 LT and collagen content (Fig. 4(b), $R^2 = 0.64$, $p = 0.016$), and SB2 LT and cell number (Fig. 4(c), $R^2 = 0.61$, $p = 0.04$).

A multivariable linear regression model of all biochemical testing data against fluorescence LT

Biomedical Optics EXPRESS

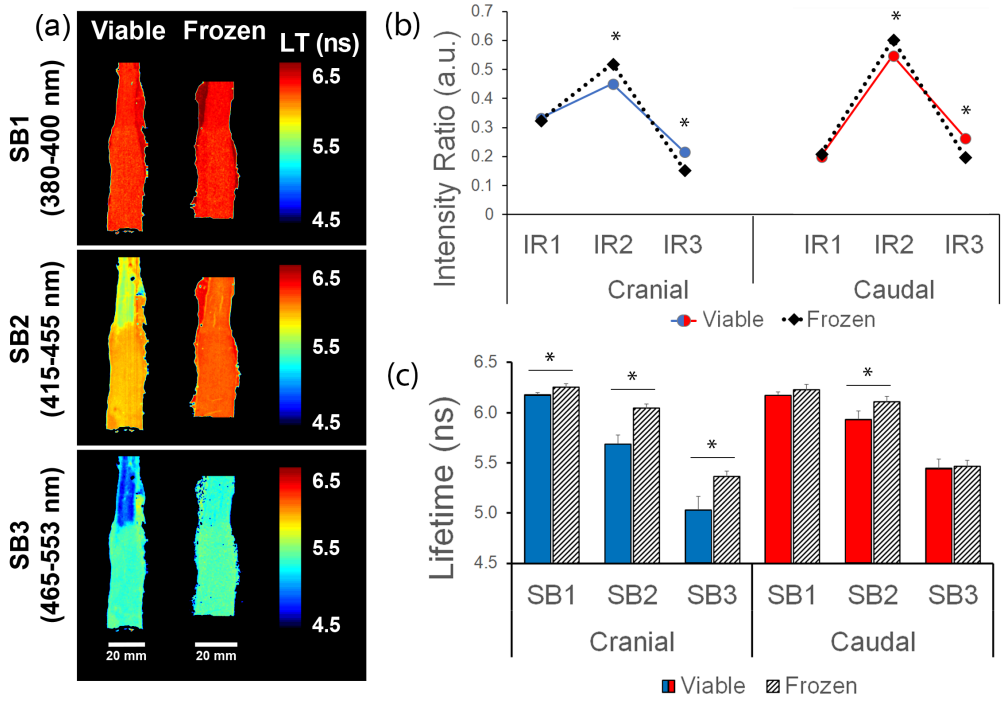

Fig. 5. Freezing alters optical properties. (a) Representative fluorescence lifetime images of a viable porcine carotid artery (viable) and after three freeze-thaw cycles at -20 °C (frozen). Quantification of the intensity ratio(b) and the fluorescence lifetime (c) in the cranial and caudal regions of the arteries before and after freezing.

data (SB1, SB2, SB3) showed that cell number had a significant negative effect on SB2 LT values (Fig. 4(d); $p = 0.05$), and increased collagen content significantly increased SB2 LT values ($p = 0.04$). Elastin content did not have a significant effect on SB2 LT values ($p = 0.41$). Increased elastin content significantly increased SB3 LT values ($p = 0.02$). Collagen and cell content did not have significant effects on SB3 LT values ($p = 0.90$ and $p = 0.45$, respectively). Collagen content, cell number, and elastin content did not have significant effects on SB1 LT values ($p = 0.18$, $p = 0.13$, and $p = 0.86$, respectively).

3.4. Freeze-thaw processing produces wavelength specific changes in carotid arteries

Freeze-thaw processing resulted in wavelength specific changes in optical properties (Fig. 5(a); representative LT images of viable and frozen samples). Freeze-thaw processing in both cranial and caudal regions of the artery resulted in a blue-shift in the intensity ratio with respect to fresh tissue, as indicated by significantly increased IR2 and significantly decreased IR3 (Fig. 5(b)). Quantification of FLIm LT (Fig. 5(c)) showed significant increases in all three spectral bands in the cranial region and a significant increase in SB2 in the caudal region with freeze-thaw processing as compared to viable tissue (Table 3).

4. Discussion

The results of the present study demonstrate the applicability of using label-free, fiber-based FLIm to quantify variations in collagen content, elastin content, and cell number in vascular tissue. The optical assessments were supported by strong linear correlations between biochemical

Biomedical Optics EXPRESS

Table 3. **Effect of freezing on fluorescence lifetime in the cranial and the caudal regions of pig carotid arteries (mean ± std; matched t-test p-values; n = 3 /group).**

Spectral band	Cranial ΔLT (ps)	*p*-value	Caudal ΔLT (ps)	*p*-value
SB1	70 ± 30	**0.04**	50 ± 20	0.2
SB2	360 ± 80	**0.003**	180 ± 30	**0.04**
SB3	330 ± 110	**0.02**	20 ± 40	0.8

assays and FLIm-derived parameters. The novel findings of this experiment include quantitative relationships between 1) increased elastin content and increased SB3 LT, 2) increased collagen content and increased SB2 LT, and 3) increased cell number and decreased SB2 LT. A fiber-based, multispectral fluorescence lifetime imaging system provides a nondestructive platform for evaluating endogenous fluorescence of tissues with three key attributes: 1) it is rapid (8 ms/pixel), 2) it has an unconstrained field of view (it can image small and large samples), and 3) it is flexible to adapt to challenging applications like intravascular imaging. The results of this study are particularly exciting because they serve as an initial step toward the creation of a nondestructive diagnostic technique for intravascular tissue-engineering applications.

The use of naturally occurring anatomical variations in collagen to elastin ratio in the carotid artery allowed two objectives to be achieved: 1) the evaluation of physiologically relevant tissue compositions in their native configuration, and 2) the optical characterization of samples with varying levels of matrix contents and biochemical properties. Porcine carotid arteries adapt their morphology and biochemical composition to fulfill the biomechanical requirements at different anatomical locations. The diameter of the carotid artery decreases from the caudal to the cranial region [47] as we observed in our samples (Fig. 2(a)-(b), Fig. 3(a)-(b), Fig. 5(a)). The elastin content in the vessel wall progressively decreases from the heart (caudal region) toward the head (cranial region) [22, 23] which we measured as a 2.4 fold decrease in elastin content in the cranial region (Fig. 2). The collagen to elastin ratio increases from the caudal region toward the head [27] which we observed as a result of the increasing elastin content in conjunction with a slight decreasing trend in collagen content along the length of the artery (Fig. 2). Utilizing the naturally occurring anatomical variations in artery biochemistry proved effective in creating a range of biochemical properties for optical characterization.

The changes in biochemical composition translate to changes in the fluorescence properties of the vessel wall. The cranial region of the arteries possessed a stronger IR1, indicative of higher concentrations from collagen content and associated crosslinking [10, 22, 48]. The caudal region had stronger IR2 suggesting stronger fluorescence contributions from elastin content (Fig. 3(a) and (c)). In general, the caudal region also featured higher fluorescence lifetime values (Fig. 3(b) and (d)).

In the low-range emission wavelengths used in this study (SB1), there were no significant differences in the fluorescence lifetime values between the cranial and caudal regions of the carotid arteries, which may be attributed to a stable ratio of collagen and crosslinks throughout the length of the artery.

The mid-range emission wavelength bandwidth (SB2) featured complex fluorescence lifetime patterns with competing contributions from collagen, elastin, and cells. Fluorescence lifetime values in SB2 had significant positive correlations with collagen content and negative correlations with cell content. Increased collagen content in the ECM tends to dominate the fluorescence lifetime in SB2 due to its intrinsic high LT value with respect to other matrix proteins. The contribution of cell number to fluorescence lifetime signal is constrained to the two inner layers of the artery by the penetration depth of the imaging system ($< 300\ \mu$m). The inner most layer, the tunica intima, is comprised of a thin layer of endothelial cells while the middle layer, the

Biomedical Optics EXPRESS

tunica media, contains smooth muscle cells. Because these cell types have shorter fluorescence lifetime values than ECM proteins in the 400 - 500 nm range [11], a relative increase in cell content shortens the measured lifetime values in SB2. The relative ratios of cellular and ECM components dictate the ultimate tissue fluorescence properties in this band.

The higher-range emission wavelength (SB3) displayed the most characteristic and consistent differences in fluorescence lifetime between the two regions of the artery. The cranial region had shorter fluorescence lifetime values (5.14 ± 0.09 ns) than the caudal region (5.5 ± 0.1 ns) for all measured samples. These significant differences in fluorescence lifetime values can be attributed to the presence of elastin, which we measured to be significantly higher in the caudal region of the carotid arteries. Elastin reportedly has a broad spectral bandwidth extending well into SB3, while collagen fluorescence is more narrow and blue-shifted with lower contributions to SB3 parameters [48, 49]. The ability of FLIm to infer the changes in elastin content in the pig carotid arteries was supported by the strong linear correlations between fluorescence lifetime in SB3 and elastin content.

As the vascular system matures, the ECM rearranges and stiffens creating age-dependent changes in the collagen to elastin ratio [27, 37, 50]. Our results indicate that the fluorescence lifetime parameters of carotid arteries from younger pigs differed from those of older animals (Fig. 3(b), P4 versus P1-3). The younger carotid arteries had longer fluorescence lifetime values in SB1 and shorter lifetime values in SB2 and SB3 when compared to the older pigs and may reflect the age-dependent ECM modifications.

The FLIm results obtained after freeze-thaw processing reflect the composition and structural changes within the extracellular matrix of the carotid arteries. Upon freezing, the cellular content decreases as cells lyse, and the collagen fibers thicken and separate from each other during dehydration and ice formation [35, 36]. These effects are more strongly manifested in the cranial region of the artery due to its higher collagen content [51] and can be observed in the lower anatomical differences in the FLIm SB2 LT values (Fig. 5(a)).

This study shows that a fiber-optic implementation of fluorescence lifetime imaging can highlight the differences in fluorescence properties between native and cryopreserved tissue. The fiber-based geometry is highly desirable because of its compatibility with intravascular imaging in tissue-engineering applications to monitor vessel maturation in a bioreactor, or *in vivo* to evaluate the cardiovascular repair and health of humans and animals. *In vivo* obstacles to FLIm involving pulsatile flow and the presence of blood have been overcome with the use of a catheter-based flushing system [15]. Moreover, a fiber-based implementation is compatible with optical coherent tomography [7, 10, 16] and intravascular ultrasound [15, 18, 19], which can be used to obtain simultaneous structural information of the tissue under examination.

5. Conclusion

In conclusion, label-free fluorescence lifetime imaging implemented with an optical fiber probe successfully detected collagen, elastin, and cellular variations in porcine carotid artery composition in both viable and previously frozen tissues. Using multivariable linear regression models, FLIm-derived parameters were found to be strongly correlated with the biochemical properties of the tissue. Specifically, the fluorescence lifetime in the spectral band 415-455 nm (SB2) detected changes in collagen content and cell number, while spectral band 465-553 nm (SB3) detected changes in elastin content. A fiber-based FLIm system has the ability for intravascular evaluations in a number of applications including intraluminal monitoring of vascular tissue graft maturation in bioreactors and *in vivo* evaluation of surgical therapeutics. The development of novel diagnostic techniques with the potential to monitor variations in biochemical composition and provide benchmark indicators of tissue maturation is an exciting step forward for both *in vitro* and *in vivo* studies.

Biomedical Optics EXPRESS

Funding

National Institutes of Health (NIH) (5R01HL121068-03).

Acknowledgments

We would like to acknowledge the help of Caleb Sehnert at the UC Davis Meat Lab and the pigs.

Disclosures

The authors declare that there are no conflicts of interest related to this article.